# RICOCHET: Scalable Passive Beamforming for mmWave Networks Using Reflectarrays

John Nolan, Xinyu Zhang

University of California San Diego

{jmnolan, xyzhang}@ucsd.edu

*Abstract*—Millimeter-wave (mmWave) technologies have seen explosive growth in the past few years with bleeding edge solutions offering unprecedented communication capacity. Unfortunately, they also introduce new challenges such as limitations in range, coverage blind spots and severe disruptions due to blockages from obstructions. Reconfigurable intelligent surfaces (RIS) have been used to alleviate some of these problems. However, RIS solutions create additional problems such as limited NLoS range and complicated beam management protocols making it incompatible with 5G. In this paper, we propose RICOCHET, a fully passive, PCB-fabricated reflective surface which uses reflect-arrays for far-field communications. RICOCHET can re-steer and reshape incidental mmWave signals towards anomalous directions to divert around obstructions, and generate wider/narrower or multi-beam patterns to fill coverage holes. To overcome the reflect-array's lack of reconfigurability, we introduce post-fabrication techniques that enable incremental deployment of RICOCHET to adapt to environment/specification changes, enhancing the SNR or broadening the coverage of an existing surface. We further design a multi-user algorithm that enables multiple transmitters to share the same RICOCHET surface while avoiding interference. Our experiments with 5G towers and WiGig access points, demonstrate that RICOCHET can effectively improve coverage without any modification to existing network infrastructure or mobile devices.

## I. INTRODUCTION

The millimeter-wave (mmWave) spectrum has garnered significant attention in the past decades, expanding its usage across a variety of application scenarios such as 5G broadband communication and automotive radar. The spectrum between 24 and 100 GHz has seen an explosive rise in popularity due to unique advantages including low licensing fees, larger communication bandwidth, smaller device footprints, *etc.* The appetite for wire-speed connectivity extends to the wireless local area network with WiGig promoting the 802.11ad/ay standards offering throughput above 100 Gbps. Ultimately, if vendors want to offer highly demanding mobile applications such as volumetric video delivery, mmWave access becomes the only feasible choice.

Moving into the mmWave spectrum poses new challenges for wireless carriers and device vendors, the biggest being limited coverage. The severe propagation losses that mmWave communication links experience require the use of phased array antennas and directional beamforming. Directionality inadvertently creates spotty coverage throughout a serviceable region. Currently, 5G mmWave customers are connected less than 1% of the time [1], [2]. The rest of the time, customers rely on complimentary low frequency links, often at lower rates. In addition, mmWave signals cannot easily penetrate or diffract around objects creating blackout zones. This phenomenon leads to increased blockages and disruptions

that interfere with communications in dynamic environments, hindering the wide adoption of mmWave technologies.

In this paper, we explore a passive reflecting surface design called RICOCHET, to tackle the mmWave coverage problem. RICOCHET is a thin, battery-free, chipless, reflect-array surface [3], fabricated using printed-circuit-board (PCB) technologies. Unlike ordinary metallic surfaces, RICOCHET can reflect and redirect stray incident mmWave signals to *non-Snellian* directions. It can also reshape the reflected electro-magnetic wave-front by creating large beamwidth scattering patterns or multi-arm patterns to illuminate hard to reach blind spots. The thin form-factor allows RICOCHET to be mounted onto building facades or roadway facilities to accommodate a variety of communication use cases. In addition, because RICOCHET is battery-free, it can be made arbitrarily large which is paramount for long range mmWave applications.

RICOCHET reflects (*i.e.* "richochets") incident far field signals to desired directions by properly designing the reflection coefficient of each metallic patch, acting like an antenna element. The geometry of each patch determines its reflection coefficient, which in turn causes a phase shift to incidental signals. By packing a large number of patch elements on the same surface, RICOCHET essentially forms a passive phased array that can resteer beams to desired directions and reshape them into desired patterns.

Unlike active relays [4], [5] or base stations (BS) which can reconfigure their beamforming settings on the fly, RICOCHET is passive and its reflection beam pattern is fixed after fabrication, so it is applicable to scenarios where the signal source and target coverage regions are predefined. This limitation can be mitigated through a *panel combining* and *fan beam combining* technique, which allows incrementally adding new surfaces to form an "array of reflection surfaces". By properly spacing the surfaces to ensure coherent combining of signals along the desired direction, the beamforming gain of the existing deployed surface can be improved. Alternatively, by using a quadratic phase profile, multiple surfaces/panels can together expand the angular coverage in a given region.

Furthermore, typical mmWave scenarios may involve multiple transmitters (*e.g.*, 5G BS) nearby, whose signals may impinge upon the same RICOCHET surface and cause inadvertent mutual interference. To overcome this challenge, we develop a *multi-user synthesis algorithm* which allows RICOCHET to accommodate multiple transmitters arriving from different incident directions and redirect them to arbitrary locations. RICOCHET can even form a null to suppress interfering transmitters while amplifying the desired one.

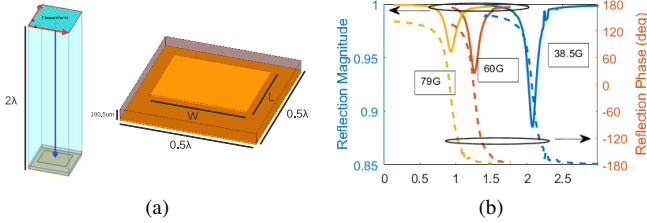Lastly, aside from static, point-to-point links, mobile sce-

Figure 1: RICOCHET patch antenna unit element. (a) Patch antenna Unit Cell (b) Amp/Phase vs. length ($L$ mm)

narios require on-the-fly configuration of beam patterns which can be challenging to deploy. Through simulation using a 3D ray tracer, we show that a distributed set of RICOCHET surfaces can greatly improve mobile, mmWave 5G performance. Specifically, by proper placement and design of the RICOCHET fan-beam patterns, we show mobile coverage can be improved in dense urban environments. We further compare RICOCHET to a distributed set of active reconfigurable intelligent surfaces (RIS) [6] which can update reflection beam patterns in real-time. We demonstrate that RIS mmWave coverage is diminished in comparison to RICOCHET, due to the beam scanning overhead and limited surface area which is constrained by cost.

To summarize, the main contributions of RICOCHET are:

*(i)* A practical end-to-end design process for large reflect-arrays.

*(ii)* Post-fabrication optimization mechanisms which allow RICOCHET to further improve link SNR or expand coverage, by incrementally adding reflection surfaces while ensuring coherent combination of the reflected signals.

*(iii)* A multi-user synthesis algorithm that allows for multiple sources to take advantage of the same reflective surface and redirect beams to arbitrarily desired angles.

*(iv)* Implementation and field testing of RICOCHET demonstrating its effectiveness and compatibility with existing 5G/WiGig mmWave networks at 39 GHz and 60 GHz, comprised of 18×18 to 164×194 antenna elements each.

*(v)* Experiments using a high-fidelity commercial ray-tracing simulator demonstrating the feasibility of accommodating device mobility using distributed passive reflect arrays.

## II. RICOCHET REFLECT ARRAY DESIGN

### A. Antenna Element Characterization

The antenna element selection is the most critical design component of a reflect array because it impacts fabrication complexity and performance metrics such as gain and bandwidth. To reduce cost and fabrication complexity, RICOCHET adopts a single layer, rectangular patch antenna array, etched onto an Isola Astra MT77 substrate with a thickness of 190.5 $\mu$m (7.5mils). The MT77 is an RF/mmWave substrate which reduces the antenna element's resistive loss [7], [8], thus providing higher gain and radiation efficiencies. Furthermore, MT77's low dielectric constant allows for larger antenna bandwidths [9]. The Astra MT77 was used for all RICOCHET designs (ranging from 38 to 79 GHz) because of the material's

stable dielectric constant at mmWave frequencies, simplifying the design and fabrication process for RICOCHET.

With the selected antenna element, we need to characterize it's reflection coefficient, *i.e.*, generating a look up table (LUT) that maps the antenna geometry to its phase shift. To reduce phase errors and maximize beamforming accuracy, it is important to ensure a sufficiently wide phase range (typically $300°$ or more [10]) which can be obtained by using different antenna geometries. We opt for FEM analysis using Ansys HFSS 3D electromagnetic simulator which allows for geometrical parameter sweeps to extract the reflection phase shift vs. geometry curves, thus populating the LUT.

The FEM model used in HFSS is shown in Fig. 1a where a rectangular patch antenna unit cell is analyzed using a single Floquet Port. Floquet analysis takes advantage of the periodicity of the electromagnetic fields in many-element antenna arrays to reduce the simulated model size [11]. The surrounding air box in the simulation is $0.5\lambda \times 0.5\lambda \times 2\lambda$ which ensures proper excitation of the fundamental Floquet modes. The reflection coefficient, $\Gamma$, of the Floquet port is calculated at the surface of the patch antenna element to extract the corresponding phase shift, *i.e.* $\angle\Gamma$. We keep the element width a constant ($2751\mu$m, $1776\mu$m, $1342\mu$m for 38.5, 60 and 79 GHz respectively) while varying its length. From Fig. 1b, we see that *all three types of patch elements used in* RICOCHET *(for 38.5, 60, and 79 GHz) have a sufficiently large phase range ($> 300°$).*

### B. Constructing a RICOCHET Reflect Array

A RICOCHET surface may consist of thousands of unit elements, each acting as a passive phase shifter with a specific geometry. When an incident plane wave arrives from a direction $(\phi_i, \theta_i)$, each element will reflect the wave with different phases. Together, they will produce a reflection pattern at a desired direction $(\phi_r, \theta_r)$ which can be modeled as:

$$A(\phi, \theta) = \sum_{a,b=1}^{N} e^{-j\vec{k_i} \cdot \vec{r_{ab}}} \cdot e^{-j\vec{k_d} \cdot \vec{r_{ab}}}, \qquad (1)$$

where $\vec{k_i}$, $\vec{k_d}$ are the incident and desired wave vectors respectively, $\vec{k} = 2\pi(\cos\phi\sin\theta, \sin\phi\sin\theta, \cos\theta)/\lambda$ and $r_{ab} = (x_{ab}, y_{ab}, 0)$ is the location of the element in the $a$-th row and $b$-th column within the 2D array. The desired wave vector defines the phases which produces the reflection pattern at the desired reflection direction plus the conjugate of the incident plane wave phases, *i.e.*,

$$\vec{k_d} \cdot \vec{r_{ab}} = \gamma \vec{r_{ab}} - \vec{k_i} \cdot \vec{r_{ab}} \qquad (2)$$

where $\vec{\gamma}_{r_{ab}}$ are the phases of each element within the array. The phase vector, $\vec{\gamma}_{r_{ab}}$ generates the desired reflection pattern.

### C. Beam Pattern Synthesis

RICOCHET can generate a variety of beam patterns to accommodate different deployment scenarios. Without loss of generality, we focus on 3 categories: *(i) pencil beam*, which concentrates the reflected signal power towards a single direction to cover a single spot far away; *(ii) fan beam* which spreads the signal power across a wide angle to form a fan shape (or cone in 3D), thus covering a wide angular area at

the cost of lower gain; *(iii) multi-arm beam*, a middle ground between the above two, which spreads the reflected signal power across multiple pencil beams or fan beams pointing in different directions.

A pencil beam can be generated following a closed-form equation based on classical antenna theory [12] where the phase weight of each unit element can be found by:

$$\vec{\gamma}_{r_{ab}} = -\vec{k} \cdot \vec{r_{ab}}. \qquad (3)$$

The phases are then mapped to the unit element geometries following the LUT. The phase weights used to generate generic fan beam patterns follow a simple quadratic model [13]: $\alpha x^2$, where $x$ represents the element index and $\alpha$ is a parameter for selecting the fan beam width. To steer the fan beam towards a desired direction, we can simply apply an additional linear phase gradient to the phase weights following Eq. (3) such as:

$$\vec{\gamma}_{r_{ab}} = \alpha x^2 - \vec{k} \cdot \vec{r_{ab}}. \qquad (4)$$

On the other hand, flat-top fan-beam, multi-arm and other more sophisticated beam patterns do not allow for closed-form solutions. To find the optimal set of phase weights, $\vec{\gamma}_{r_{ab}}$, that achieve a desired beam pattern, we adopt a simple differential-evolution genetic algorithm (DE-GA). We first randomly initialize the phase weights, and then interatively search for the best set of weights that satisfies a cost function. Specifically, $\vec{\gamma}_{r_{ab}}$ is randomly generated and used to calculate $\tilde{A}(\phi, \theta)$ which is then compared to a desired beam pattern. The best performing subset of phase weights which minimizes the delta between $\tilde{A}(\phi, \theta)$ and $A(\phi, \theta)$ are propagated to the next iteration where they are updated with "mutations". This process continues until convergence.

For large RICOCHET array designs, instead of solving for optimal phase weights for the entire array which is computational expensive, we optimize the azimuth and elevation dimensions separately, which reduces the problem domain to two, 1D phase vectors instead of a 2D problem. This simplifies the simulation and reduces the convergence time.

### D. Link Budget Analysis

When constructing a RICOCHET array, a link budget analysis is necessary for ensuring that the reflection performance is sufficient to achieve the desired mmWave coverage. The governing model for link budget analysis is the bi-static radar cross section (RCS) equation which models signal propagation when an intermediate reflector is involved [14]:

$$P_r = \frac{P_t G_t G_r \lambda^2 \sigma}{(4\pi)^3 d_T^2 d_R^2} \qquad (5)$$

where $P_r$, $P_t$, $G_t$, $G_r$, $\lambda$, $d_T$, $d_R$ and $\sigma$ are the received signal strength (RSS), transmit (Tx) signal power, Tx gain, receive (Rx) gain, wavelength in freespace, TX-to-object distance, RX-to-object distance and the *RCS* of the surface, respectively. The key design knob of RICOCHET is its RCS, *i.e.*, $\sigma$, which is determined by the size of the surface, and can be derived by extending the RCS model of a flat metallic plate [15]:

$$\sigma = \frac{4\pi(D_x D_y)^2}{\lambda^2} \cdot \frac{0.886}{D_x \theta_x} \cdot \frac{0.886}{D_y \theta_y} \cdot \frac{1}{N_{beams}^2} \qquad (6)$$

where the first term defines the electrical size of the 2D array,

*i.e.*, $D_x = d_x N_x$, $D_y = d_y N_y$ being the array spacing times the number of elements along $x$ and $y$. The second and third term define the beamwidth of the array, $\theta_x$, $\theta_y$ relative to the maximum beamwidth for the given array size, $D_x$, $D_y$. The last term defines multi-arm beam patterns which split power among multiple beams pointing to different directions, hence reducing per beam RCS.

From Eq. (6), it may be tempting to simply increase the size of the RICOCHET surface to achieve a higher RCS. However, the trade offs to this are increased costs, decreased beamwidth and exponentially diminishing RCS returns which could pose challenges for practical deployment. In addition, the reflection power does not grow indefinitely with the surface size or RCS. Instead, it is limited by the amount of incidental power, which in turn is capped by the free space path loss model [1], [9]. So the maximum usable RCS is:

$$\sigma_m = \frac{4\pi(d_T d_R)^2}{(d_T + d_R)^2}. \qquad (7)$$

If the required RCS (Eq. (5)) to satisfy the communication/sensing link exceeds $\sigma_m$, then RICOCHET will not be able to meet the link budget. Otherwise, we can safely follow Eq. (6) to determine the size of the RICOCHET surface.

### E. Scalable RICOCHET Design

RICOCHET is a fully passive device, so it is more difficult to reconfigure once the design has been fabricated and installed. In this section, we propose two techniques that can flexibly scale up an existing RICOCHET surface to increase its beamforming gain or expand its angular coverage.

**Panel combining.** The communication or sensing environment may change after RICOCHET is deployed, requiring larger surfaces for extended range for example. To improve the beamforming gain of an already deployed surface, and accordingly enhance the link SNR, we introduce a panel combining (PC) scheme which allows for incremental deployment of additional RICOCHET panels (*i.e.*, surfaces). The additional RICOCHET panels however, cannot simply be mounted immediately adjacent to the existing panel. A proper offset is needed to ensure *phase coherency between panels*. The phase difference between the two identical panels should be constant:

$$\gamma_C = \vec{\gamma}_{r_{ab}}|_{2N} - \vec{\gamma}_{r_{ab}}|_{N+N} \qquad (8)$$

where $\vec{\gamma}_{r_{ab}}|_{2N}$ are the weights found using a surface of $2N$ elements, and $\vec{\gamma}_{r_{ab}}|_{N+N}$ are the weights of a surface composed of two identical sub-surfaces each with $N$ elements using weights found using Eq. (2). The phase difference can be removed by introducing a distance offset that provides the necessary phase shift. For placement of multiple panels along the $x$ or $y$ axis respectively the distance offset is calculated:

$$d_x = \frac{-Nkd_a(\cos \phi_i \sin \theta_i + \cos \phi_r \sin \theta_r) \mod 2\pi}{kd_a(\cos \phi_i \sin \theta_i + \cos \phi_r \sin \theta_r)}, \qquad (9)$$

$$d_y = \frac{-Nkd_b(\sin \phi_i \sin \theta_i + \sin \phi_r \sin \theta_r) \mod 2\pi}{kd_b(\sin \phi_i \sin \theta_i + \sin \phi_r \sin \theta_r)}, \qquad (10)$$

where $N$, $k$, $d_{a,b}$, $\theta_i$, and $\theta_r$ are the number of elements in the array, the wave number, element spacing, incidence angle and reflection angle, respectively of the already installed surface.
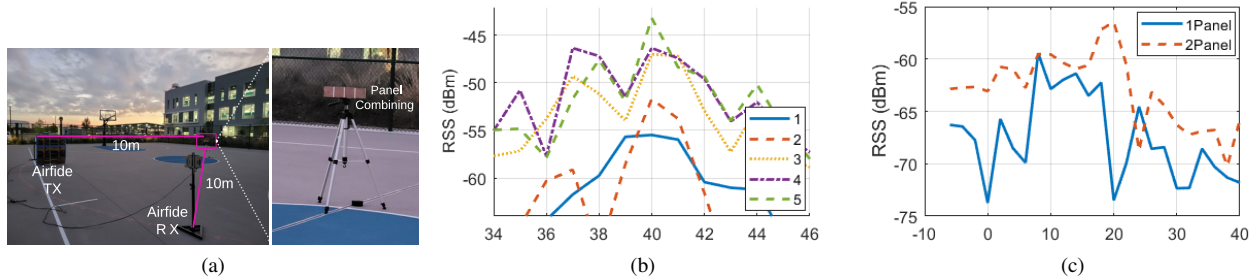
Figure 2: (a) Experimental setup for PC, FB combining, MB, and a close-up image. (b) RSS gain vs. number of panels. vs. azimuth coverage (deg) (c) Coverage gain of fan-beam combining. (deg)

The intuition behind this is that the phase error induced by placing a second panel directly next to a preexisting one (*i.e.* Eq. (8)) is a fixed value that applies to all elements in the second panel. By placing the second surface relative to the first with the above offset distance, the required phase coherency is achieved. All additional panels (*i.e.*, more than two) simply need to adhere to this distance relative to the adjacent panel to achieve coherent combining. Note that the above closed-form panel combining only works for pencil beam designs, since the phase offset (*i.e.*, distance) between panels is well defined for a single incidence and reflection direction only, *i.e.*, $[(\phi_i,\theta_i),(\phi_r,\theta_r)]$. If the design specifications (*e.g.*, incidence or reflection angle) change, a new RICOCHET design is needed with a different spacing.

To verify the panel combining technique, we fabricate five identical 36×36 RICOCHET surfaces at 60 GHz following Sec. II-B. The measurements were conducted outdoors as shown in Fig. 2a using 802.11ad radios. The incidence angle is $(\phi_r,\theta_r)$=(270°,20°). For phase coherency following Eq. (10), a distance of 9.736 mm is used to separate each additional panel and the RSS is measured along the reflection directions.

As shown in Fig. 2b, the RSS of each additional panel at the desired reflection angle of $(\phi_r,\theta_r)$=(90°,40°) is approximately increased by $N_{panels}^2$ in linear scale, indicating that the reflected signals are coherently combined. As the number of panels increases, the main-lobe becomes narrower making measurements more difficult due to antenna misalignment. As a consequence, the measured RSS becomes weaker than expected. Furthermore, the relative RCS gain tapers off as more panels are installed, requiring an impractical amount of additional panels when a very large RCS is desired.

**Fan-beam Combining.** In addition to boosting the link SNR, a practical deployment may need to expand the angular coverage of reflected signals, and ideally an incremental upgrade is preferable. To meet this requirement, we propose a fan-beam (FB) combining scheme, where additional panels can be installed to preexisting RICOCHET surfaces to broaden the reflection beam, following the closed-form model discussed in Sec. II-C. Knowing the previously installed RICOCHET panel information to generate the fan-beam, such as number of unit elements $N$, and the coefficient $\alpha$, additional panels can simply be installed by extending the quadratic phase profile (Sec. II-C). In other words, the phases of the additional panels can be found by $\alpha x^2$ with $x = N + 1, N + 2, \cdots, N + M$ where $M$ is the size of the new array.

To evaluate the fan-beam-combining concept, we fabricate two RICOCHET panels with 36×36 unit elements each for use at 60GHz. One panel has a symmetric quadratic phase profile $\alpha x^2$, with $\alpha$=0.84375. This phase profile generates an approximately 15° fan-beam. The combined surfaces were designed to reflect an incident plane wave arriving from $(\phi_i,\theta_i)$=(270°, 20°) and reflect the fan-beam towards $(\phi_r,\theta_r)$=(90°,-6 to 26°). As shown in Fig. 2c, a single symmetric fan-beam panel produces a pattern which spans approximately 8° to 18°. The reason for not reaching the 26° could lie in multiple factors, such as leakage interference from the specular reflection which appears at 20° creating a null, and other interference sources such as the tripod assembly. However, when the second panel is installed following our fan-beam combining method, the coverage extends beyond 8° down to -6°. The improvement in the positive angular range, which now extends to 24°, could be due to the realignment of the panels changing the interference dynamics from the specular reflection. Instead of creating a null at 20°, it constructively interferes with the reflection from the two panels, creating a strong peak and extending the angular coverage as desired. These techniques do not require BS or UE modifications or synchronization between them.

## III. FACILITATING POINT-TO-POINT MMWAVE LINKS

mmWave back-haul links can benefit from RICOCHET by leveraging the extended coverage and range [16]. As these links are point-to-point, RICOCHET surfaces can be deployed on roof tops or tall buildings to aid in circumventing back-haul blockages, reducing deployment costs.

**Extending WiGig coverage.** To verify RICOCHET's ability to expand coverage and range we now conduct experiments using 60GHz WiGig hardware to verify the design process in Sec. II. We deploy a mmWave link using a commodity 60 GHz WiGig radio from Airfide [17]. The radio has a built-in phased array, follows the standard beam scanning protocol in 802.11ad, and is configured to testing mode to transmit a single tone. We fabricate five RICOCHET designs, with 18×18, 36×36, two 72×72 and a 216×72 elements, all with 0.5λ spacing of antenna elements along $x$ and $y$ dimensions. The 216×72 design measures 640mm×180mm.

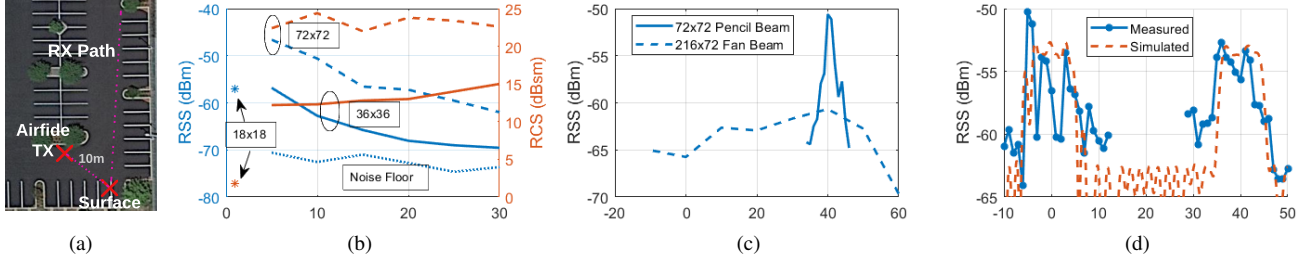The remaining square designs, with 18, 36, and 72 elements

Figure 3: (a) WiGig scenario using parking lot. (b) RCS/RSS vs Distance (meter), 18x18, 36x36 and 72x72 element surfaces. (c) Pencil/Fan vs azimuth angle (deg) as measured in parking lot. (d) Multi-arm beam vs angle (deg) as measured in Fig. 2a.

per edge, measure 45×45, 90×90, and 180×180mm, respectively. The three square designs were fabricated to reflect an incident plane wave from $\phi_i,\theta_i = (270,20)°$ towards $\phi_r,\theta_r = (90,40)°$ which is 20° off from the specular reflection direction *i.e.* non-Snellian. The second 72×72 design reflects a multi-arm pattern with two fan-beams directed towards 0° and 40°. The last design reshapes the pattern into a 60° fan beam covering the azimuth angles from -10° to 50°. The reflection phases for the square designs, *i.e.*, $\vec{\gamma}_{r_{ab}}$ in Eq. (2), were composed of two 1D phase vectors, zero phase in the x dimension, and y given by $(0,y\pi sin(\theta_r))$, with $\theta_r = 40°$. This phase vector generates a pencil beam pointing to $\phi_r,\theta_r = (90,40)°$. The 216×72 element design uses a quadratic phase vector with $\alpha = 0.42$ and $x \in [-108, 107]$.

The RICOCHET surfaces are mounted onto a tripod 10 m away from the Airfide radio. Using a handheld spectrum analyzer and a horn antenna, the received signal strength (RSS) is measured along a linear trajectory from 1 m to 30 m following the 40° reflection angle as shown in Fig. 3a. The Airfide radio's effective isotropic radiated power (EIRP) is 24 dBm according to the spectrum analyzer measurement.

Fig. 3b shows that the 36×36 and 72×72 pencil beam designs maintain RCS values above 13 and 23 dBsm respectively throughout the linear region, which approximately matches the theoretical model in Eq. (6). The 18×18 surface covers a maximum distance of 1 m due to the insufficient RCS and low EIRP, limiting the distance. Despite the limitation, the RCS of 3 dBsm matches that of Eq. (6). The discrepancy of the 72×72 RCS is due to the narrow beamwidth making antenna pointing difficult which could result in lower RCS/power levels than expected. Nonetheless, a single 180×180mm (72×72) RICOCHET surface was able to redirect a signal 30 meters with a theoretical range of 70 meters following 5 before the signal is drowned by noise.

We now demonstrate various coverage-related use cases of RICOCHET such as point-to-point communications or blind spot filling. Using a spectrum analyzer, Fig. 3c plots the pattern of the pencil beam reflected by the 72×72, in comparison to the broad 60° fan beam reflected by the larger 216×72 surface. These results match the design specification and the link budget model in Sec. II-D. Although the 216×72 element design is 3× larger, its RCS is relatively low due to the spreading of the energy across the 60° beam. Such a design can fill large coverage holes. On the other hand, the narrow

beamwidth 72×72 surface can concentrate power at a specific direction for fixed NLoS point-to-point links.

To validate the multi-beam 72×72 surface, we set up an Airfide transmitter and receiver on a basketball court as shown in Fig. 2a. Multi-beam designs can be used to connect multiple mmWave back-haul links. The measured RSS vs. reflection angle using the Airfide receiver as opposed to the spectrum analyzer used previously, is plotted in Fig. 3d. Two strong fan-beam peaks appear at 0 and 40° as expected.

The two nulls present in the left fan beam are most likely caused by TX side-lobe leakage from the TX slightly blocking the RX. Specifically, since the fan-beam edge (-5°) is close to the incidence angle of the transmitter (-20°), the RX has to be placed close to the TX and unavoidably receives side-lobe energy. In addition, the Airfide RX uses a single quasi-omni patch antenna which compounds the multi-path interference. In spite of this imperfection, the multi-arm pattern may be more desirable than an overly large fan beam if signal power is only desired in specific directions, *e.g.*, in 5G fixed wireless access networks where a BS serves two homes. Multi-beam designs can keep the RICOCHET surface relatively small, while still achieving large per-beam gain and long range. For example, the RCS of the multi-beam design following Eq. (6) is 12.7 dBsm, whereas the 216×72 element design, which is physically 3× larger, is only 3dB higher in RCS.

**Expanding 5G Coverage.** 5G mmWave networks leverage the 28 GHz or 39 GHz frequency bands to achieve up to 5 Gbps of downlink throughput [18]. Similar to automotive radar, 5G links can suffer from blockages and coverage blind spots due to civilian infrastructure such as buildings. Providing adequate coverage in hard to reach areas is impractical for wireless ISPs due to the logistics and cost of installing 5G mmWave BSs. Using the RICOCHET surface, the BSs' signals can be easily resteered and reshaped towards the NLoS coverage holes, which equivalently reduces the infrastructure density and cost. *In addition,* RICOCHET *reflects signals for both downlink and uplink in a reciprocal manner, and does not require modifications to existing BS/UEs, or network protocols.* RICOCHET does not require a separate control channel for configuration or additional beam training. So it affords a quick, deployable, and low-cost service unlike RICOCHET active counterparts [19], [20].

We now demonstrate this capability through a field test in a Verizon 5G mmWave network which resides on the 38.5 GHz
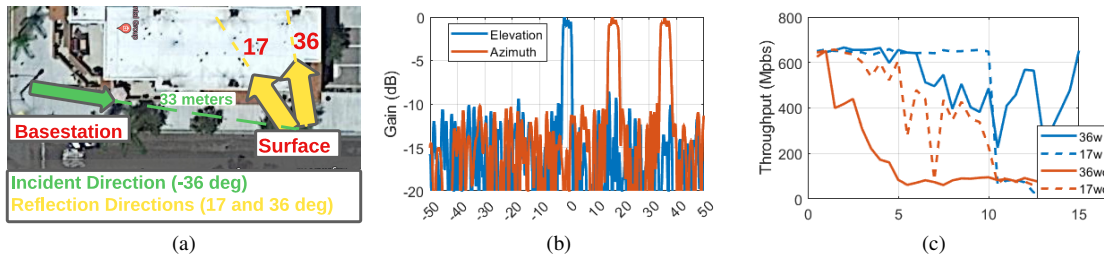
Figure 4: (a) Field test of RICOCHET in Verizon's 5G mmWave network. (b) Gain Patterns (deg) of the RICOCHET reflectarray. (c) Throughput measurements across distances (meters).

frequency band. Our experimental setup aims to emulate the "wireless fiber-to-home" deployment scenario, where the ISP aims to replace the traditional DSL or fiber access links with 5G mmWave links. We first pinpoint a 5G mmWave BS based on the coverage map of the local urban area provided by Verizon. As shown in Fig. 4a, the BS is located at the corner of an intersection on a light pole 33m away from an opening in a parking garage. Using a commodity 5G phone (TCL 10), we found that the UEs located inside the garage cannot access the mmWave service due to the NLoS conditions. To alleviate this issue, we place a single RICOCHET surface (455mm×607mm) in the LOS of the BS to redirect and reshape the signals towards the inside of the garage. As an example, we assume two target blind spots are located along the azimuth angles of 17° and 36°, respectively, relative to the RICOCHET surface as shown in Fig. 4a with yellow arrows. The height of the Verizon BS was measured using a measuring tape, laser and elevation data from [21]. The incident angle was found to be 10° in elevation and −36° in azimuth.

To determine the surface configuration following Sec.II, we note that a rigorous link budget analysis for the 5G links is quite difficult given the unknown details of the proprietary cellphone performance and BS capabilities.

Despite this, we make a set of assumptions based on common configurations, *e.g.*, a BS EIRP of 33 dBm [22], a cellphone receiver antenna gain of 10dB, noise figure (NF) of 10dB [23] with 100MHz bandwidth and a required SNR of 20 dB for 64QAM modulation. Besides covering the two Azimuth blind spot angles, we note that the elevation beamwidth should not be too narrow. Otherwise minor height deviation of the surface may result in significant signal gain variation. We empirically set the elevation angle to be 3° which should provide height tolerance for typical link distances. Following Eq. (5), we set the minimum surface RCS to be 22 dBsm to achieve a minimum SNR of 20dB at the UE. We design a 117×156 element surface with two 3° fan beams pointed at 17° and 36° as shown in Fig. 4b, corresponding to an RCS of 24dBsm (Eq .(6)) which meets the derived requirement.

Using the TCL 10 smartphone, we measure the downlink throughput via Google SpeedTest [24], following two linear trajectories along the 17° and 36° azimuth angles with 0.5 m spacing between measurement points. The results in Fig.4c show that, without the RICOCHET surface, the UE can still establish mmWave connections with the BS, likely owing to

obstacle penetration, multi-path reflections and diffractions. However, the link throughput varies sporadically across locations, and falls quickly over distance, *e.g.*, near 0 throughput beyond 5 m along the 17° trajectory.

In contrast, with the RICOCHET surface, the link throughput is consistently higher until around 11 m. Similarly, along the 36° path, the RICOCHET link throughput is consistently above 200 Mbps and even higher throughput is re-established at 15 m. Without the RICOCHET surface, the link throughput immediately starts to taper off as the UE enters the NLoS region, and is completely disconnected from the mmWave network service around 5 m (indicated by the service code on the Android phone), suggesting that the signal level is too weak even with multi-path or diffraction.

## IV. MULTI-USER MANAGEMENT

The above RICOCHET design has focused on a single transmitting source reflecting off of a RICOCHET surface. In real world scenarios, multiple transmitters may coexist, each with its own desired coverage region. We thus introduce a multi-user synthesis (MUS) algorithm which can generate RICOCHET surfaces to accommodate multiple links.

Simply combining surfaces with different incidence and reflection angles does not work in practice as large ripples and specular reflections will interfere [25]. In general, to accommodate $N$ BSs, RICOCHET must generate beam patterns with $N$ arms. Each arm reshapes a BS's signal towards a desired reflection direction. MUS leverages the fact that when signals arrive from a different incidence angle than the initially designed angle, a reflection pattern shift occurs which can be modeled analytically. When another transmitter's signal arrives from a different incident angle, MUS will shift the initial reflection pattern and align an arm to the desired reflection direction. Essentially, MUS *creates multiple spatial channels by creating a multi-arm pattern that connects all the transmitters with their respective receivers by leveraging the reflection pattern shifting property*. This allows for multiple links to concurrently utilize RICOCHET with the only limitation that the multiple arms of the reflection pattern not intersect.

The shifting phenomena can be derived from Eq. (1), where $\vec{k_i}$ is now different from what was used to design the RICOCHET array. Specifically, Eq. (1) and (2) now have different incident phases. The 1D angular beam shifting caused by differing incidence angles from the initially designed angle, can be modeled as:
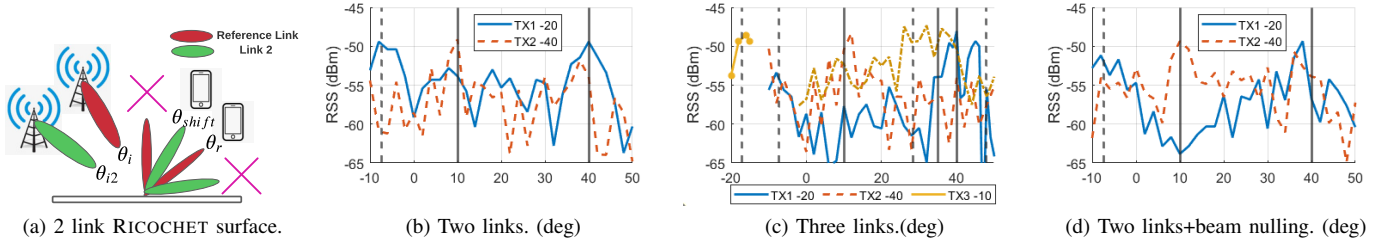
(a) 2 link RICOCHET surface.
(b) Two links. (deg)
(c) Three links.(deg)
(d) Two links+beam nulling. (deg)

Figure 5: Experimental results for MUS.

$$\theta_{shift} = \arcsin(\sin(\theta_i) - \sin(\theta_{i2}) + \sin(\theta_r)), \qquad (11)$$

where $\theta_{shift}$, $\theta_i$, $\theta_{i2}$, and $\theta_r$, are the new beam location after shifting, the initially designed incident angle, the new incident angle causing the shift, and the reflection angle of the initially designed surface, respectively. In other words, $\theta_r$ shifts to location $\theta_{shift}$ due to the change of incident angle from $\theta_i$ to $\theta_{i2}$ as shown in Fig. 5a. This property can be utilized to generate an initial multi-arm pattern with $N$ arms that can properly shift the location of the arms with known varying incidence angles. To construct a RICOCHET multi-user design, an initial TX/RX link ($\theta_i$,$\theta_r$) is used as the reference design following Sec. II-B, but with a multi-arm pattern with arms located at:

$$\theta_{preshift} = -\arcsin(\sin(\theta_{init}) - \sin(\theta_i) - \sin(\theta_r)), \qquad (12)$$

one for each of the remaining links, where $\theta_{preshift}$ is the location prior to shifting due to the differing incidence angle. The initial multi-arm pattern containing the reference TX/RX link and the pre-shifted beams, forms an *N-arm* beam pattern which is synthesized using Sec. II-C.

The *N-1* remaining TX/RX links each create a newly shifted *N-arm* pattern where one of the arms aligns the pattern to satisfy the TX/RX link directions. As an example, two TX/RX links $[(\theta_{TX1},\theta_{RX1}),(\theta_{TX2},\theta_{RX2})]$, with $[(-20, 40), (-40, 10)]$ will form two multi-arm patterns with two beams each where the reference reflection angle of $40°$ has been shifted to $70.6°$ due to the incidence angle of $-40°$ being used in the second link. Similarly, the pre-shifted beam location of $-7.3°$, shifted to $10°$ which is the desired reflection direction for the second TX/RX link.

Note that in actual communication networks such as 5G, multiple UEs can be covered by the same reflection beam while multiplexing the channel in time/frequency. In addition, the MUS can be adapted to suppress interfering beams. For example, suppose the two links shown in Fig. 5a are at similar distances to the RICOCHET surface, but the first link transmitter outputs a higher EIRP than the second. The power reflected towards the non-desired user could drown that coming from the desired second transmitter. Using the same pattern synthesis method as in Sec. II-C, we can create a "null" beam towards the non-desired user to suppress interference.

To verify the feasibility of MUS, we conduct experiments on three RICOCHET 72×72 designs, which accommodate 3 cases: 2 links, 3 links, and 2 links with mutual interference.
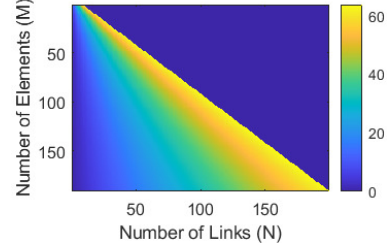


Figure 6: Percentage of interfering beams when sharing the same RICOCHET surface.

The TX/RX link definitions are $[(-20, 40), (-40, 10)]$ following an additional link, (-10,35) for the 3-link design. The results in Fig. 5b show the desired reflection directions of the 2-link beams, where the solid black lines represent the reflection directions for the incident directions of -20° and -40°. The dotted black line highlights the undesired beam that is generated as a consequence of the multi-arm requirement for multi-user access. In a similar fashion, the 3-link design maintains the desired 2-link reflection angles in addition to the desired reflection angle of 35° for an incidence angle of -10°, as shown in Fig. 5c. In addition, the extra unwanted beams are shown with dotted black lines and are located close to desired beams which matches Eq. (11).

We further experiment with a 2-link mutual interference case, where a reflection beam points to the desired receiver at $10°$, but a high-EIRP interferer's signals leak to the same direction. Using the aforementioned beam nulling method, we synthesize a null to suppress the interference. As shown in Fig. 5d, the null located at $10°$ creates an approximately 15 dB interference margin, which suffices to ensure a high quality link at the desired receiver. The experimental results verify the effectiveness of the MUS and the accuracy of the model (*i.e.*, Eq. (11) and Eq. (12)) behind it.

**Limitations of MUS.** Despite the capability of supporting multiple BSs, MUS does bear a few restrictions:
*(i) RCS decreases with $N^2$.* As discussed in Sec. II-D, specifically Eq. (6), the RCS of a RICOCHET surface decreases with the number of reflection arms. To compensate for the RCS reduction with $N$ arms, the surface would need to be made $N$ times larger, which entails higher cost and more space.
*(ii) Potential interference between adjacent BSs.* To accommodate $N$ BSs nearby, RICOCHET needs to produce $N^2$ reflection arms. As $N$ becomes large, it becomes challenging to ensure none of the the redundant arms interferes with an undesired receiver. To better understand the interference limitation, we

(a) Downtown Boston Map.

(b) Throughput 6 Passive RICOCHET Surfaces

(c) Throughput 3 Active MetaSurfaces

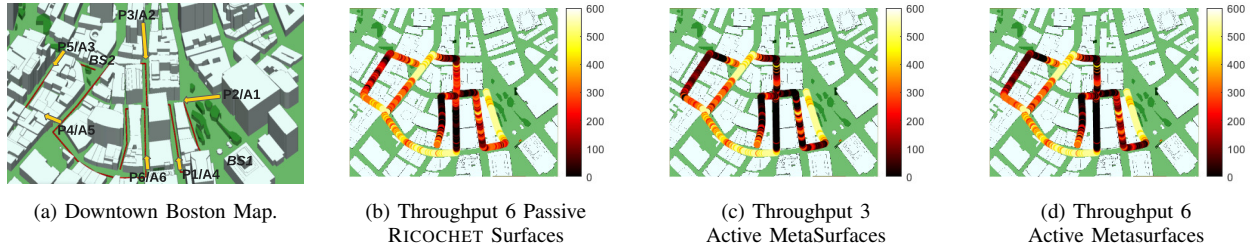(d) Throughput 6 Active Metasurfaces

Figure 7: A comparison between the distributed passive reflectarrays and active metasurfaces.

conduct a Monte-Carlo simulation, where incidence and reflection angles within the RICOCHET surface's FoV (-70° to 70°) are assumed to be uniformly distributed to model many BS locations. The simulation calculates the percentage of average interference over 10,000 iterations caused by the unwanted arms vs. the antenna array size, $M$, and vs. the number of MUS links, $N$. An $M$ element array can produce approximately $M$ arms or less [14]. Interference will occur if an unwanted beam from one of the $N^2 - N$ arms falls within the first-null-beam-width of a desired direction. The results are shown in Fig. 6. As the array size $M$ and number of BSs $N$ increases, the percentage of the beams causing interference approaches approximately 63%. As $M$ grows, the maximum number of transmitters that the array can achieve increases as well. Simultaneously, the multi-arm beamwidth that can be utilized reduces, allowing for more beams to be packed within the FoV of the RICOCHET surface. As $N$ grows however, the likelihood of interference increases as well due to the beam shifting following Eq. (11). As $N$ approaches a large value, the redundant arms have higher probabilities of interfering with one of the $N$ desired beams. The probability approaches 63% for arrays up to 200 elements long and up to 200 simultaneous transmitters. For small $N$ in a given deployment scenario, interference can be avoided through proper network planning with known BS locations and target blind spot regions.

## V. DEALING WITH MOBILITY USING DISTRIBUTED RICOCHET SURFACES

RICOCHET is ideal for expanding fixed wireless access – currently the major campaign of 5G mmWave carriers [26]. We emphasize however, that RICOCHET surfaces can indirectly facilitate mobile UEs as well by illuminating a target mobility region through a wide-angle fan-beam in both azimuth and elevation. Due to the reciprocal nature of passive beamforming, a UE located within the fan-beam's coverage will redirect its uplink signals to the BS through RICOCHET. Effectively, fan-beams mitigate the MUS reflection angle shifts by illuminating a wide angular region. In addition, RICOCHET can work seamlessly with existing 5G mmWave devices without any modifications to the network stack. With multiple RICOCHET surfaces covering different blind spots, a BS can perform beam scanning and automatically "choose" the surface providing best SNR to each mobile UE, similar to how it chooses natural reflectors for NLoS coverage.

To verify mobility under RICOCHET, we use Wireless InSite (WI), a 3D EM ray-tracing tool, to examine the coverage

and network capacity of a mobile mmWave 5G network [27]. WI has been widely used for simulating large electromagnetic environments and their impact on 3D propagation dynamics such as multi-path by considering practical antenna patterns and reflections/diffractions from the surrounding objects [27]–[32]. In [33] specifically, WI was compared to outdoor measurements, showing good agreement between the two. Our simulation, as shown in Fig. 7a, takes a 3D model of downtown Boston as an input scenario and deploys two 5G mmWave BSs. The red lines represent the moving trajectory of a vehicle UE. To cover the urban streets, we deploy 6 passive RICOCHET surfaces (denoted as $P_i, i \in [1,6]$) which generate flat top fan-beam patterns in both azimuth and elevation. The surfaces are spread around within LoS of the nearest BS. The yellow arrows in Fig. 7a depict the pointing direction of each surface. The position, azimuth (Az) and elevation (El) beamwidth (BW), and tilt angle of each surface are determined beforehand to maximize the coverage of the streets. All RICOCHET surfaces consist of $144 \times 144$ elements except for $P_3$ which has $500 \times 500$. Following Sec. II-D, the surface sizes are designed to ensure a minimum 20 dB SNR at all points within the FoV, which end up to be $77 \times 77$ $cm^2$–only slightly larger than the one in our 5G field test (Fig. 4a). The BS transmit power and beamforming gain is assumed to be 37 dBm and 24.5 dB respectively, common for Power Class 1 BSs which use a 64 element phased array for beamforming [34]. To compare the performance between RICOCHET and RIS, we simulate a $35 \times 35$ element RIS which is $3 \times$ the size of the state-of-the-art design in [20], [35] ($20 \times 20$) which, to our knowledge, is the largest RIS demonstrated on the 5G band. The active surfaces are placed at the same location as the passive surfaces and are denoted as $A_i, i \in [1,6]$. The simulated active RIS uses a codebook with 60 pencil-beam, beamforming directions evenly distributed within its FoV providing maximum gain. This is common for deployed mmWave BSs today [36], and is a hard constraint that aims to limit the beam searching overhead of active beamforming arrays.

WI simulates the multiple reflections and diffractions created by various BSs and surfaces deployed within the scenario. At each UE location, the SINR is calculated and mapped to achievable throughput based on the 3GPP specification for mmWave FR2 with 100 MHz bandwidth. Fig. 7b shows that across the UE's moving trajectories using a mono-pole antenna pointed in the direction of travel, RICOCHET maintains an average throughput of 273 Mbps and a total of 93 outages

(*i.e.* 0 Mbps at a location) out of 768 locations, compared to an average of 222 Mbps and 258 outages using the 5G mmWave BSs alone. By merely using 3 passive surfaces per BS, RICOCHET increases the average UE throughput by 23%, and reduces the outage ratio by 64%!

Considering that a 0.46m×0.61m surface was fabricated and tested in the 5G field test Fig.4a, the simulated surface sizes are not out of the realm of possibility and would not be any more difficult to design and fabricate. The major limitation however, is when the distance between the BS and surface is too great such as for $P_3$ which at a distance of 310m from the BS and at a height of 130m above the ground, requires a surface size of 2.68m×2.68m which could be an eyesore and difficult to install. Note that RICOCHET works in the far-field of the transmitter and the target region. The theoretical far-field distance ($2D^2/\lambda$ where $D$=diameter) is only a rule-of-thumb for pencil beams. For fan/multiarm beams, the far-field becomes shorter, comparable to a smaller surface with the same gain. Sec. III confirms that the beam pattern forms properly at much shorter distances than theory given that a 640mm×180mm surface was measured at 10m successfully due to the fan-beam.

It may be tempting to believe that RIS will be superior to RICOCHET in mobile scenarios. To demystify the differences, we first simulate 3 RIS deployed at locations $A_2$, $A_3$, and $A_5$, respectively. We expect the RIS' cost of deployment and maintenance will total at least double that of RICOCHET due to sophisticated hardware and the need for external power. We compare this deployment with the aforementioned 6 RICOCHET surfaces. From the results in Fig. 7c, we find that RICOCHET improves average throughput by 18.7%, and reduces the outage ratio by 50.5% compared to RIS. To examine the best case performance of RIS, we further simulate an ideal RIS with 6 deployed surfaces. The results are shown in Fig.7d. We observe that RICOCHET still achieves higher average throughput (14.2% larger), and much higher reliability (39.2% lower outage ratio), compared with the ideal RIS.

To summarize, a distributed set of passive RICOCHET surfaces can potentially provide ubiquitous coverage for 5G mmWave networks. The performance of RICOCHET is superior to a practical active RIS deployment, and even better than an ideal RIS surface which is much costlier and more complex. The smaller surface sizes of RIS designs will limit the outdoor use case scenarios due to the limited reflected power compared to larger passive surfaces.

## VI. RELATED WORK

**Metasurfaces.** RIS, an extension to metasurfaces containing active circuitry to reconfigure the reflection response, [19], [37] have been developed in recent years to manipulate wireless channels and extend the network coverage. For example, polarization control [38] and reflect/transmit control [39] have been used to improve coverage. Though reconfigurable at runtime, RIS' rely on digital circuitry to control the elements, and require real-time channel measurements as input to make the control decisions. Several systems [19] assume a wire-

line control channel between the RIS and the BS/UE which constrains the practical deployment. Other works propose channel measurement based approach to select the reflection beam [39]. However, due to lack of synchronization with the BS, these surfaces can hardly maintain the required rapid beam switching (*e.g.*, 125 $\mu$s per beam for 5G [40]). Furthermore, RIS are heavily limited in size due to the manufacturing cost and complexity, which in turn limits their reflection power. This issue is exacerbated at higher frequencies such as mmWave. The size constraint is also due to the need to limit the number of available beams and the associated beam searching overhead. We show in the previous sections that a few passive RICOCHET surfaces can already achieve similar coverage as active surfaces even under mobility, Sec. V.

**Expanding mmWave Coverage.** Designs such as X-Array [41] seek out to improve mmWave coverage by combining many active phased arrays. Existing active RIS systems [42], [43] only work when the reflecting surface is a few meters away from the transmitter due to the aforementioned problems of complexity and limited size scalability. In [44], a 28GHz RIS is designed and measured alongside a 5G BS that is only 2.3m away. Kitayama *et al.* are able to achieve a NLOS range of 35m whereas RICOCHET achieved 40m with a single 72×72 element passive surface. Fully passive metallic reflectors have been implemented as an alternative [45]. However, the performance and capabilities of these designs are limited to single directions and have no scalability. In addition, these metallic objects cannot reshape beams into multi-arm beams or fan-beams. thus satisfying multiple BS/UEs impossible. In [25], multiple panels are combined to produce fan-beams. Due to non-coherent phasing, the resulting fan-beam varies significantly in power within the field-of-view (*i.e.*, 5 dB variation). Moreover, due to phase errors, a large specular reflected lobe is present. Lastly, Qian *et al.* [46] use a metal-backed, 3D printed dielectric structure to enhance mmWave coverage for WiGig applications. Although cheaper than alternative solutions, the metal deposition process is tedious and the surface sizes are severely limited, reducing the range where these surfaces can provide enhanced coverage to 10m. As we detailed in the previous sections, large surface size is paramount for mmWave communication and sensing applications.

## VII. CONCLUSION

We have introduced RICOCHET, a passive mmWave reflective surface which has been experimentally verified to improve coverage for mmWave sensing and communication applications. Through full-wave analysis and PCB fabrication, RICOCHET surfaces can be designed to enhance coverage through a variety of sizes, reflection beam patterns, or through the use of MUS. We anticipate that RICOCHET and similar designs will be paramount to realizing dense mmWave networks for 5G communications and beyond.

## ACKNOWLEDGMENT

REFERENCES

[1] opensignal, "Quantifying the mmwave 5g experience in the us — july update."

[2] M. Dano", ""mmwave 5g in 2023: Fast, but still expensive and hard to find"."

[3] TICRA, "Reflectarray antenna design."

[4] S. Kinney, "Densifying mmwave 5g while managing deployment costs," 2020. [Online]. Available: https://www.rcrwireless.com/20200428/5g/how-can-mmwave-distributed-relays-expand-5g-coverage

[5] Movandi, "Movandi," 2022. [Online]. Available: https://movandi.com/

[6] W. Tang, X. Chen, M. Z. Chen, J. Y. Dai, Y. Han, M. D. Renzo, S. Jin, Q. Cheng, and T. J. Cui, "Path loss modeling and measurements for reconfigurable intelligent surfaces in the millimeter-wave frequency band," 2022.

[7] isola group, "Astra mt77," https://www.isola-group.com/pcb-laminates-prepreg/astra-mt77-laminate-and-prepreg/, 2022.

[8] I. Ndip, T. H. Le, O. Schwanitz, and K.-D. Lang, "A comparative analysis of 5g mmwave antenna arrays on different substrate technolgies," in 2018 22nd International Microwave and Radar Conference (MIKON), 2018, pp. 222–225.

[9] B. A. Constantine, Antenna theory: Analysis and Design. Wiley, 2016.

[10] J. Encinar, "Design of two-layer printed reflectarrays using patches of variable size," IEEE Transactions on Antennas and Propagation, vol. 49, no. 10, pp. 1403–1410, 2001.

[11] S. Noghanian, "Efficient and accurate simulation of antenna arrays in ansys hfss."

[12] J. D. Mahony, "On the relationship between the directivity and the half-power beamwidth in quasi-symmetric pencil-beam radiation patterns," IEEE Antennas and Propagation Magazine, vol. 54, no. 4, pp. 238–243, 2012.

[13] C. Fonteneau, M. Crussière, and B. Jahan, "A systematic beam broadening method for large phased arrays," in 2021 Joint European Conference on Networks and Communications at 6G Summit (EuCNC/6G Summit), 2021.

[14] M. Skolnik, Radar Handbook, Third Edition. McGraw Hill; 3rd edition, 2008.

[15] R. Ross, "Radar cross section of rectangular flat plates as a function of aspect angle," IEEE Transactions on Antennas and Propagation, vol. 14, no. 3, pp. 329–335, 1966.

[16] X. Ge, H. Cheng, M. Guizani, and T. Han, "5g wireless backhaul networks: challenges and research advances," IEEE Network, 2014.

[17] R. Zhao, T. Woodford, T. Wei, K. Qian, and X. Zhang, M-Cube: A Millimeter-Wave Massive MIMO Software Radio, 2020.

[18] L. Hardesty, "Verizon, ericsson, qualcomm hit 5g peak speed of 5 gbps in test."

[19] M. Dunna, C. Zhang, D. Sievenpiper, and D. Bharadia, "Scattermimo: Enabling virtual mimo with smart surfaces," in In Proceedings of ACM MobiCom, 2020.

[20] J.-B. Gros, V. Popov, M. A. Odit, V. Lenets, and G. Lerosey, "A reconfigurable intelligent surface at mmwave based on a binary phase tunable metasurface," IEEE Open Journal of the Communications Society, vol. 2, pp. 1055–1064, 2021.

[21] FreeMapTools, "Elevation finder."

[22] Anritsu, "Making eirp measurements on 5g base stations."

[23] S. Andersson, L. Sundström, and S. Mattisson, "Design considerations for 5g mm-wave receivers," in 2017 Fifth International Workshop on Cloud Technologies and Energy Efficiency in Mobile Communication Networks (CLEEN). CLEEN, 2017, pp. 1–5.

[24] Google, "speedtest."

[25] S. Hongnara, Tanan and Yoshiki, "Dual-polarized broad-beam reflective metasurface based on multi-sheet configuration for local 5g application at 28.25 ghz," in 2021 15th European Conference on Antennas and Propagation (EuCAP), 2021.

[26] FierceWireless, "Verizon adds 4 more mmwave cities, expands 5g home service."

[27] Remcom, "Wireless insite references."

[28] R. Kawecki, S. Hausman, and P. Korbel, "Performance of fingerprinting-based indoor positioning with measured and simulated rssi reference maps," Remote Sensing, 2022.

[29] A. Taha, M. Alrabeiah, and A. Alkhateeb, "Enabling large intelligent surfaces with compressive sensing and deep learning," IEEE Access, vol. 9, pp. 44 304–44 321, 2021.

[30] H. A. Obeidat, I. Ahmad, M. R. Rawashdeh, A. A. Abdullah, W. S. Shuaieb, O. A. Obeidat, and R. A. Abdallhameed, "Enhanced toa estimation using ofdm over wide-band transmission based on a simulated model," Wireless Pers Commun 123, vol. 123, p. 3449–3461, 2022.

[31] A. Alkhateeb, S. Alex, P. Varkey, Y. Li, Q. Qu, and D. Tujkovic, "Deep learning coordinated beamforming for highly-mobile millimeter wave systems," IEEE Access, vol. 6, pp. 37 328–37 348, 2018.

[32] A. Petosa, N. Gagnon, C. Amaya, M. Li, S. Raut, J. Ethier, and R. Chaharmir, "Characterization and enhancement of the environment for 5g millimetre-wave broadband mobile communications," in 12th European Conference on Antennas and Propagation (EuCAP), 2018.

[33] S. Wang, J. Huang, and X. Zhang, "Demystifying millimeter-wave v2x: Towards robust and efficient directional connectivity under high mobility," in Proceedings of the 26th Annual International Conference on Mobile Computing and Networking, 2020.

[34] litepoint, "Transitioning from dvt to manufacturing for 5g fr2 mmwave devices."

[35] M. Rossanese and Mursia, "Designing, building, and characterizing rf switch-based reconfigurable intelligent surfaces," in Proceedings of the 16th ACM Workshop on Wireless Network Testbeds, Experimental Evaluation & CHaracterization, 2022.

[36] B. Flowers, X. Zhang, and S. Dey, "Low overhead codebook design for mmwave roadside units placed at smart intersections," in 2021 IEEE 32nd Annual International Symposium on Personal, Indoor and Mobile Radio Communications (PIMRC), 2021, pp. 366–372.

[37] X. Tan, Z. Sun, D. Koutsonikolas, and J. M. Jornet, "Enabling indoor mobile millimeter-wave networks based on smart reflect-arrays," in IEEE INFOCOM 2018 - IEEE Conference on Computer Communications, 2018.

[38] L. Chen, W. Hu, K. Jamieson, X. Chen, D. Fang, and J. Gummeson, "Pushing the physical limits of IoT devices with programmable metasurfaces," in USENIX Symposium on Networked Systems Design and Implementation (NSDI 21), 2021.

[39] V. Arun and H. Balakrishnan, "RFocus: Beamforming using thousands of passive antennas," in 17th USENIX Symposium on Networked Systems Design and Implementation (NSDI 20). USENIX Association, 2020. [Online]. Available: https://www.usenix.org/conference/nsdi20/presentation/arun

[40] M. Giordani, M. Polese, A. Roy, D. Castor, and M. Zorzi, "A tutorial on beam management for 3gpp nr at mmwave frequencies," IEEE Communications Surveys & Tutorials, vol. 21, no. 1, pp. 173–196, 2018.

[41] S. Wang, J. Huang, X. Zhang, H. Kim, and S. Dey, X-Array: Approximating Omnidirectional Millimeter-Wave Coverage Using an Array of Phased Arrays, 2020.

[42] K. W. Cho, M. H. Mazaheri, J. Gummeson, O. Abari, and K. Jamieson, "Mmwall: A reconfigurable metamaterial surface for mmwave networks," in Proceedings of the 22nd International Workshop on Mobile Computing Systems and Applications, 2021.

[43] A. Albanese, F. Devoti, V. Sciancalepore, M. Di Renzo, and X. Costa-Pérez, "Marisa: A self-configuring metasurfaces absorption and reflection solution towards 6g," in IEEE INFOCOM 2022 - IEEE Conference on Computer Communications, 2022.

[44] D. Kitayama, D. Kurita, K. Miyachi, Y. Kishiyama, S. Itoh, and T. Tachizawa, "5g radio access experiments on coverage expansion using metasurface reflector at 28 ghz," in 2019 IEEE Asia-Pacific Microwave Conference (APMC), 2019.

[45] S. Chaimool, C. Rakluea, P. Sangmahamad, Y. Zhao, A. Worapishet, and P. Akkaraekthalin, "Experiment of a phase-gradient metasurface reflector for millimeter wave and 5g applications," in 2022 16th European Conference on Antennas and Propagation (EuCAP), 2022.

[46] K. Qian, L. Yao, X. Zhang, and T. N. Ng, "Millimirror: 3d printed reflecting surface for millimeter-wave coverage expansion," in Proceedings of the 28th Annual International Conference on Mobile Computing And Networking, 2022.